

## ORIGINAL ARTICLE

# Effect of Macro, Micro and Nano Loads on The Indentation Behavior of Ti-6Al-4V and Haynes 242 Alloys

B. Sridhar Babu<sup>1</sup>, A. Kumaraswamy<sup>2</sup> and Kaushik Kumar<sup>3,\*</sup>

<sup>1</sup>Mechanical Engineering Department, CMR Institute of Technology, Hyderabad - 501401, India

<sup>2</sup>Mechanical Engineering Department, Defence Institute of Advanced Technology, Pune - 411025, India

<sup>3</sup>Mechanical Engineering Department, Birla Institute of Technology, Mesra, Ranchi - 835215, India

**ABSTRACT** – Indentation tests were conducted on Ti-6Al-4V and Haynes 242 alloys at macro, micro and nano load range using conventional and depth-sensing indentation instruments to study the load effects on the mechanical behaviour of the alloys. With the increase of indentation loads from macro to nano, a decrease in Young's modulus and indentation hardness values was observed as a result of the indentation size effect in the alloys. During the loading procedure in macro, micro and nano indentations, the loading curves progressively moved upwards, showing the increase in resistance of the alloys with the increase in indentation load. Compared the depth-sensing instrumented indentation hardness of alloys with the conventional indentation hardness at micro loads, the magnitude of the depth-sensing instrumented indentation hardness is 10-25% greater than the conventional indentation hardness. The reason for this variation is explained as the depth-sensing instrumented indentation hardness is calculated at maximum load with the projected contact residual impression area,  $A_c$ , instead of the residual indenter impression projected area,  $A_r$ . So the indent pileup and sink-in play a major difference between the depth-sensing instrumented hardness and conventional indentation hardness. The outcome of the experimental work clearly indicates that for evaluation of the hardness usage of projected contact residual impression area provides more accurate results than when residual indenter impression projected area is used. The concept is synonymous to evaluation of engineering stress / strain and true stress / strain using original and actual cross sectional area respectively.

## ARTICLE HISTORY

Received: 7<sup>th</sup> Oct. 2021

Revised: 21<sup>st</sup> June 2022

Accepted: 4<sup>th</sup> July 2022

Published: 16<sup>th</sup> July 2022

## KEYWORDS

*Indentation;*

*Ti-6Al-4V;*

*Haynes 242;*

*Projected contact*

*residual impression area;*

*Residual indenter*

*impression projected area*

## INTRODUCTION

The indentation tests are the most commonly used non-destructive procedures to evaluate the mechanical behaviour of newly developed materials, and the indentation tests have the potential to be an excellent substitute for a standard tensile/compression test [1]-[5]. In the present investigation, the indentation behaviour of Haynes 242 and Ti-6Al-4V alloys are studied using conventional and depth-sensing instrumented indentation. These two alloys are most commonly used in aerospace applications because of their attractive mechanical properties. Haynes242 alloy is a nickel-based super alloy that has exceptional attractive mechanical properties because of the fine dispersion of metastable  $Ni_2$  particles. It contains 25% Mo and 8% Cr (wt %), with Ni as the balance [6]-[9]. Ti-6Al-4V alloy has two crystal structures, one is  $\alpha$  phase, i.e. Hexagonal closed-pack (HCP) and the second one is  $\beta$  phase body-centred cubic (BCC). At room temperature, pure titanium consists of 100%  $\alpha$  phase.  $\alpha$  to  $\beta$  phase allotropic transformation takes place at the 883 °C  $\beta$  transus temperature. To stabilize the  $\beta$  phase in Ti-6Al-4V, vanadium (V) is added by minimizing the  $\beta$  transus temperature and with the addition of aluminium (Al), it increases. The  $\beta$  phase transus temperature of Ti-6Al-4V with 6 wt.% of Al and 4 wt.% V is 980 °C, beyond which Ti is 100%  $\beta$ . It can be heat treated and aged [10] for its attractive and exceptional mechanical properties like the high strength–density ratio at high temperatures. Higher  $\beta$  content provides higher creep resistance.

In conventional indentation tests, the indentation load ( $P_{max}$ ) is gradually applied to the indenter and the indenter residual impression area ( $A_r$ ) is determined by using an optical microscope. The static conventional indentation hardness ( $H_s$ ) is obtained by:

$$H_s = \frac{P_{max}}{A_r} \quad (1)$$

In the depth-sensing instrumented indentation technique, the indentation hardness of the material is taken as the ratio between the maximum indentation load,  $P_{max}$ , and the projected residual indenter impression contact area,  $A_c$ , of the residual impression.

$$H_d = \frac{P_{max}}{A_c} \quad (2)$$

In depth-sensing instrumented indentation, mostly Berkovich indenter is used and its residual indentation impression area function is:

$$A_c = 24.56 h_c^2 \quad (3)$$

$$h_c = h - \gamma \frac{P_{max}}{S} \quad (4)$$

where,  $\gamma$  is Berkovich indenter geometric constant and its value is  $\gamma = 0.75$  [11] and  $h$  is the indentation depth. The slope of the unloading curve, also known as contact stiffness,  $S$ , can be expressed as:

$$S = \frac{dP}{dh} = \alpha \cdot m (h - h_f)^{m-1} \quad (5)$$

$\alpha$ ,  $m$  and  $h_f$  are the constants and  $h_c$  is the contact depth over which the indenter makes contact with the alloy. The Young's modulus of alloy,  $E$ , is calculated by:

$$\frac{1}{E^*} = \left[ \frac{1 - \nu_i^2}{E_i} + \frac{1 - \nu_s^2}{E} \right] \quad (6)$$

$$E^* = \frac{\sqrt{\pi}}{2} \frac{S}{\sqrt{A_{proj}}} \quad (7)$$

where  $\nu_s$  is the Poisson ratio, and  $E^*$  is the reduced modulus of the specimen.  $E_i=1140$  GPa,  $\nu_i=0.07$  are diamond indenter Young's modulus and Poisson's ratio values, respectively.

Static conventional indentations are mostly used up to the micro loads only because measuring the residual impression of indentation is very difficult at nano loads with a normal microscope. The advantage of depth sensing instrumented indentation is it does not require imaging of residual impression area for the evaluation of hardness. Depth sensing instrumented indentation can be used to study the behaviour of non-metallic materials like polymers [12], [13]. The accuracy of the depth-sensing instrumented hardness,  $H_d$ , depends on how fine the residual indenter impression contact area,  $A_c$ , substitutes the projected residual indenter impression area,  $A_r$ , of conventional static indentation.

Balshakov and Pharr [14] found that due to the pile-up and sink-in behaviour of the alloys, the estimation of the true contact area of the residual indenter impression,  $A_c$ , is very difficult and Sudershan [15] revealed that the Oliver and Pharr method numerical equations should be applied cautiously for the materials having  $\sigma_y/E$  ratio is 10.4 to 10.2. However, except few finite element analyses [16]-[18], Studies on experimental comparison of static conventional indentation and depth-sensing indentation hardness were very few and not up to the mark. Conventional plastic theories to the macro and nano loads have not been addressed in any of the previous investigations. The dependence of the mechanical properties on indentation load is termed as indentation size effects (ISE). A thorough understanding of the size effects and its correlation to conventional plastic theories is especially important in modern applications.

The aim of this work is to analyze the variation of hardness in static conventional indentation and depth sensing indentation and also to study the load influence on the characterization of Ti-6Al-4V and Haynes 242 alloys without considering the effect of indenter geometry. The main focus is on how the load and displacement curves, Young's modulus and hardness of alloys vary with respect to the macro, micro and nano loads and provides an explanation for load depending behaviour of the materials.

## EXPERIMENTAL DETAILS

### Materials and Microstructure

In the present investigation, Haynes 242 and Ti-6Al-4V alloys were used and the Ti-6Al-4V specimens were heated to 1232 K for one hour, then cooled in a furnace and aged for 6 hrs at 802 K followed by cooling in the atmosphere. Haynes 242 samples were prepared in as-received condition. The specimens' top and bottom surfaces were polished to mirror-like surfaces within  $\pm 0.1 \mu\text{m}$ . Figure 1(a) shows the optical microstructure of Ti-6Al-4V material with solution heat-treated and overaged (STOA). The microstructure consists of about transformed  $\beta$  and 30% primary equiaxed  $\alpha$ . The transformed  $\beta$  consists of martensite needles ( $\alpha'$ ) and a negligible amount of  $\beta$ . Figure 1(b) shows the microstructure of Haynes 242 alloy; it reveals that the Ni<sub>2</sub> (Cr, Mo) precipitates were present in an aspect ratio of 8:3 in the major, intermediate dimensions and with lenticular in shape. Mn, iron, Si, Ni and Al were observed to partition to the  $\gamma$  matrix. Cr was not found to partition extensively between the phases, and Mo was found to partition to the Ni<sub>2</sub> (Cr, Mo) precipitates.

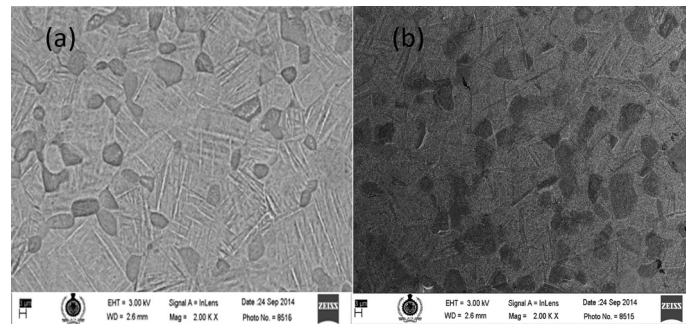


**Figure 1.** Microstructure of (a) Ti-6Al-4V (b) Haynes 242 alloys.

### Static Conventional and Depth-Sensing Instrumented Indentation Tests

Static conventional indentation experiments were conducted on Ti-6Al-4V and Haynes 242 alloys using Brinell hardness tester, Rockwell hardness tester and Vickers micro hardness tester. A spherical indenter made up of non-deformable tungsten carbide (WC) with a 2.5 mm diameter was used in the conventional Brinell hardness tester and the hardness of the spherical (ball) indenter was 220 HV. Five indentations were made on both materials using Brinell and hardness tester at a load range of 62.5 kgf to 250 kgf. In the Vickers micro hardness test, a square base pyramid-shaped diamond indenter was used and five indentations were made on both the materials at a load range of 5 gmf to 2000 gmf. The diameter of the indentations was measured using a GT-K optical microscope.

### Microindentation Test

The micro-indentation experiments were conducted on a universal mechanical tester (UMT) with a Berkovich tip. Contact stiffness load control mode (CSM) was used in micro indenter; in this mode, at regular intervals the contact stiffness can be extracted from the indentation load-depth curve. Six micro indentations were made with load control at 1750 mN load and maintained 30  $\mu\text{m}$  gap was maintained between the indents. To decrease the influence of variations in the micro indentation hardness values, the average values of six indentations have been considered representative values.

### Nanoindentation Test

Nanoindentation tests were performed on G200 Agilent nanoindenter with Berkovich indenter tip, and contact stiffness depth control mode (CSM) was applied to obtain contact stiffness at a regular load-displacement curve. A series of ten nanoindentations were conducted at 120 mN load and to eliminate the effect of point-to-point variations in the experimental nano indentation hardness results and average values all ten nano indentations have been considered as representative values.

## RESULTS AND DISCUSSION

### Indentation Load and Displacement Curves

The static and depth-sensing indentation load and displacement curves of Ti-6Al-4V and Haynes 242 alloys are shown in Figure 2(a), 2(b), 3(a) and 3(b), respectively. During the loading procedure in both types of indentations, the loading curves gradually moved upwards, indicating increase in resistance of the alloy with an increase in load. Variations of the indentation depths depend on the resistance of the material against deformation, and due to variation of dislocation density, there is an increase in the indentation depth with an increase in indentation loads. As per Figure 2(a), the load and displacement curves of Haynes 242 alloy, the high initial unloading slope and a very small recovery in indentation depth suggest that the alloy possesses high contact stiffness and Young's modulus.

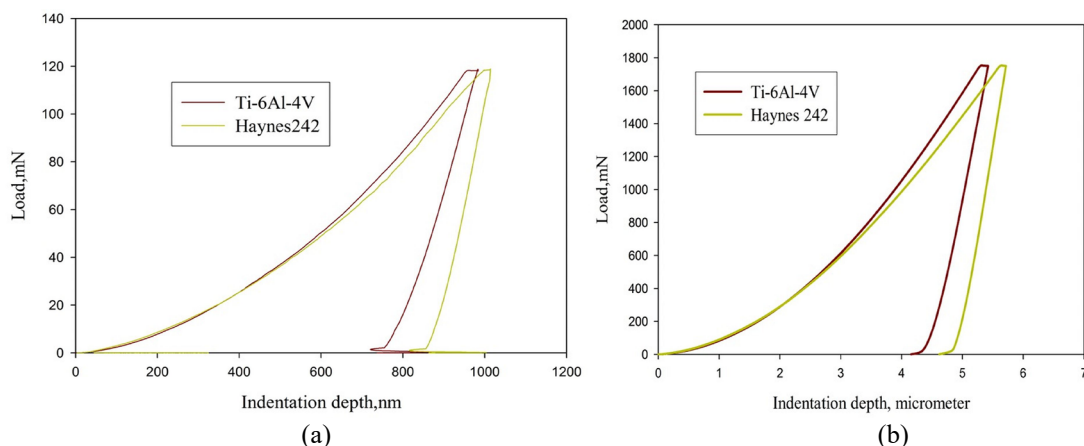


**Figure 2.** Depth sensing indentation load and displacement curves of (a) nanoindentation at 120 mN load and (b) micro indentation at 1250 mN load.

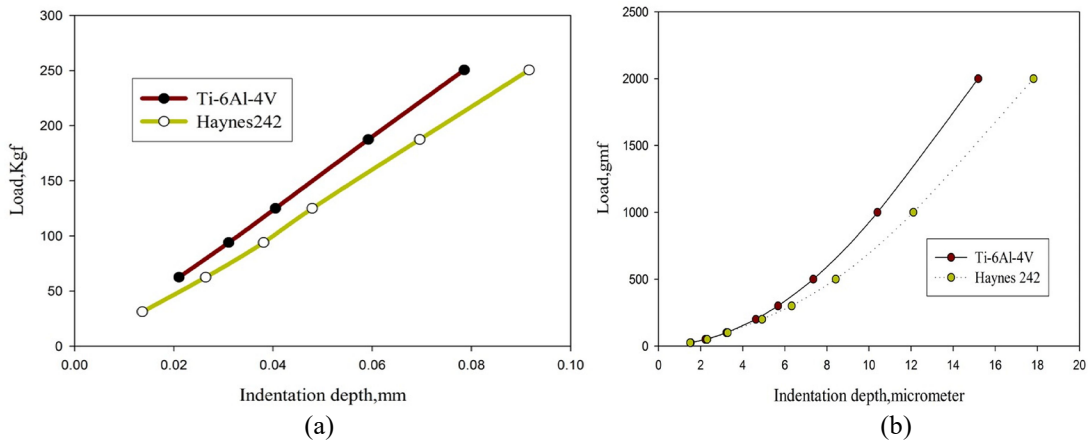


**Figure 3.** Static indentation load and displacement curves of (a) Brinell hardness test and (b) Vickers micro hardness test at micro loads.

**Static Conventional and Depth Sensing Instrumented Indentation Hardness of Alloys**

The variation of static conventional indentation hardness at macro and micro loads has been plotted for Ti64 and Haynes 242 alloys in Figure 4. Static conventional indentation hardness,  $H_s$ , for the alloys has been calculated using the Eq (1); this hardness can be termed as Mayers hardness. With indentation load, the static conventional hardness was observed to sudden increase at macro indentation loads due to the strain hardening effect but at micro loads the hardness is gradually decreasing in both alloys.

The variation of depth-sensing instrumented indentation hardness,  $H_d$ , at 120 mn (nano load) and 1750 mn (micro load) with respect to the indentation depth has been plotted for Ti64 and Haynes 242 alloys in Figure 5. The hardness values are calculated using Eq. (2). At nano and micro loads there is a decrease in indentation hardness with the increase in depth of indentation. The percentage of decrease in hardness at nano load is very high compared to the variation of hardness at micro load, indicating more indentation size effects at nano load. The residual impression of Berkovich indenter in depth-sensing indentation is shown in Figure 6.

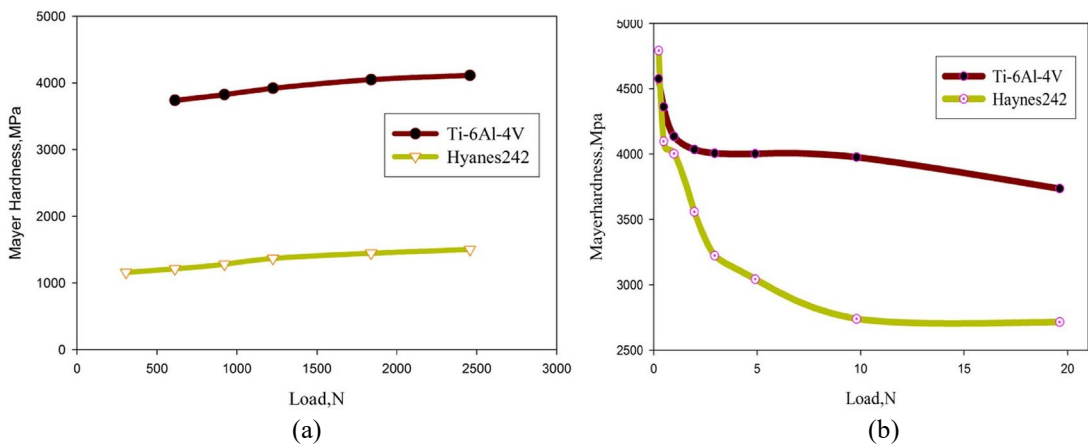


**Figure 4.** Static indentation hardness at (a) macro loads and (b) micro loads.

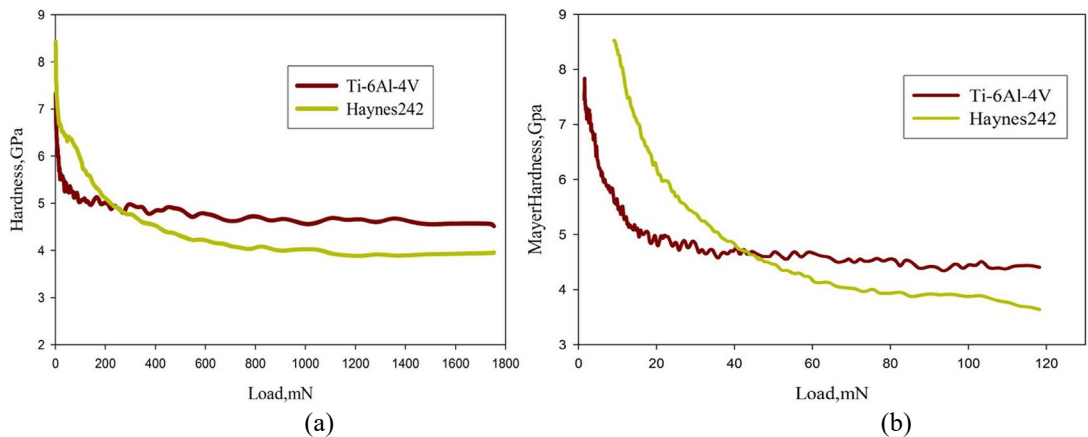


**Figure 5.** Depth sensing indentation hardness at (a) micro loads and (b) nano loads.

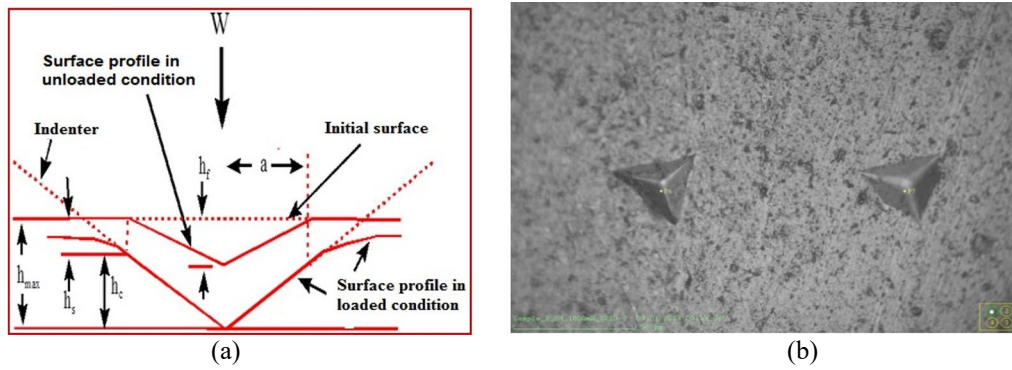


**Figure 6.** Berkovich indenter residual impression for (a) line diagram and (b) experimental impression.

**Macro, Micro and Nano Load Effects and Comparison of Static Conventional and Depth Sensing**

The effect of indentation loads on instrumented indentation hardness,  $H_d$ , for both the alloys is shown in Figure 5. Clearly, the  $H_d$  of Haynes 242 appears to have the strongest load effect. The  $H_d$  of Ti-6Al-4V exhibits a weak load effect compared to the Haynes 242. This load effect on the indentation values is generally called as the indentation size effect (ISE). Variation in the indentation hardness due to indentation size effects was explained due to the strain hardening effect in the materials. The Young’s modulus of both alloys are shown in Figure 7. With the increase of load from macro to nano, there is a decrease in the Young’s modulus,  $E$  values. The consistent decrease in the  $E$  values of alloys may be due to the evolution of micro cracks around the indent [19]. Whereas, Figure 4 and Figure 5 show the experimental results of depth sensing indentation hardness and static hardness are very sensitive to the indentation size effects and the variation is 10% to 25%, demonstrating that the depth-sensing instrumented indentation hardness depends on the resistance against deformation.

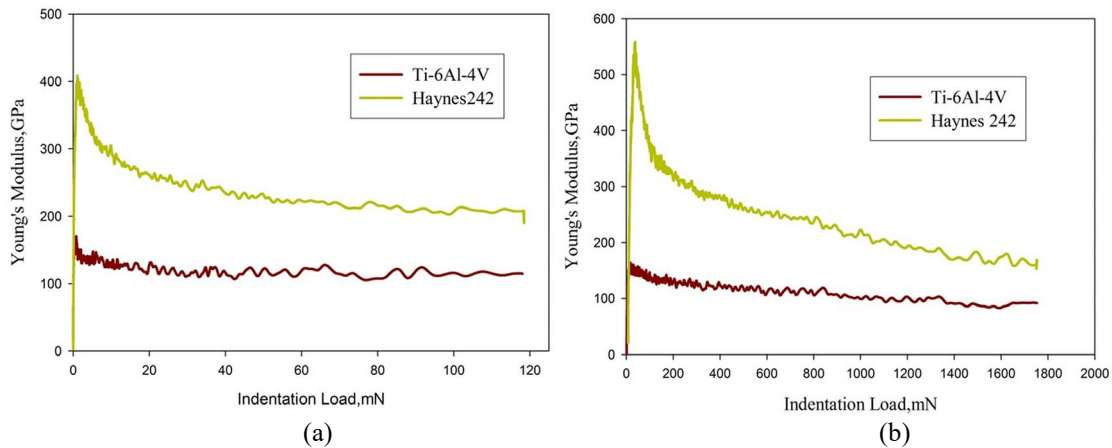


**Figure 7.** Variation of Youngs’s modulus at (a) nano load and (b) micro load.

Oliver Pharr method was used to calculate the depth-sensing instrumented indentation hardness  $H_d$  from the indentation load and displacement curves, as discussed in the introduction. The  $H_d$  describes the resistance against deformation of the material. In Figure 8, for both alloys, the static hardness  $H_s$  values are less than the  $H_d$  values. To show the variation quantitatively, the ratio of  $H_s$  and  $H_d$  are presented in Table.1. As per these values, the  $H_d$  values are 10 to 20% higher than the static hardness. Using FE analysis Bolshakov and Pharr concluded that the real contact indent area,  $A_r$ , with the pile-up made the area greater than  $A_c$  from the Oliver Pharr (O&P) numerical procedure. This, in turn main reason for the high magnitude of depth-sensing indentation hardness values. But the materials with small Y/E show the pile-up and sink in effect, so the main reason for variation is attributed to the depth-sensing indentation hardness values which are calculated using projected residual indent impression contact area  $A_c$  instead of residual indenter impression projected area  $A_r$ .

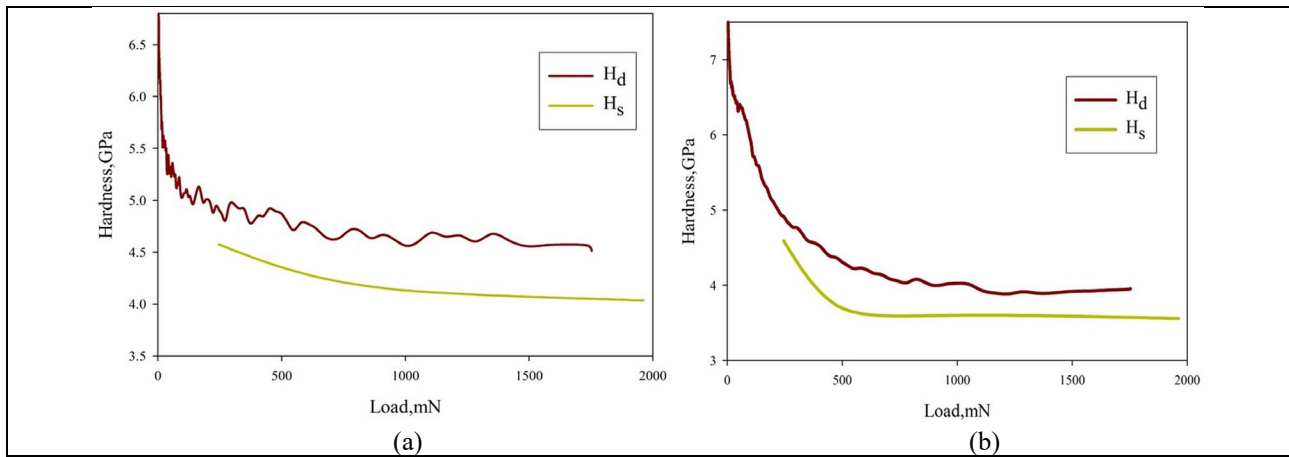


**Figure 8.** Comparison of the static and depth-sensing hardness of (a) Ti-6Al-4V and (b) Haynes.

**Table 1.** Comparison of the  $H_d$  and  $H_s$ .

SNo	Material	E (GPa)	Y (GPa)	Y/E	$H_s/H_d$
1	Ti-6Al-4V	105	0.998	0.009	0.869
2	Haynes 242	195	0.780	0.004	0.898

## CONCLUSION

The work was targeted to analyze the variation of hardness in static conventional indentation and depth-sensing indentation. The scope also included a study of the load influence on the characterization of Ti-6Al-4V and Haynes 242 alloys without considering the effect of indenter geometry. It can be concluded that the depth-sensing instrumented indentation hardness of the alloys was found to be larger than the static conventional hardness values. It can be inferred that the depth-sensing instrumented hardness of alloys appears to be strong indentation size effects compared to the static conventional indentation hardness. The main reason for the variation in the hardness can be attributed to the analysis of the depth-sensing indentation hardness using the projected contact residual indenter impression area,  $A_c$ , instead of the residual projected indenter impression area,  $A_r$ . But the nature of loading curves, i.e. continuously increasing, indicates that for both types of indentation, there is an increase in resistance of the alloys with the increase in indentation load.

## ACKNOWLEDGEMENT

The authors sincerely acknowledge the comments and suggestions of the reviewer(s) and editor(s) that have been instrumental for improving and upgrading the paper in its final form.

## REFERENCES

- [1] J. Dean, and T.W. Clyne, "Extraction of plasticity parameters from a single test using a spherical indenter and FEM modeling," *Mech. Mater.*, vol. 105, pp. 112–122, 2017, doi: 10.1016/j.mechmat.2016.11.014.
- [2] C. Schneider-maunoury, and A. Albayada, "On the use of instrumented indentation to characterize the mechanical properties of functionally graded binary alloys manufactured by additive manufacturing," *Mater. Today Commun.*, vol. 25, pp 101-108, 2020, doi: 10.1016/j.mtcomm.2020.101451.
- [3] D. Tabor, *Hardness of metals*, Oxford: Clarendon Press, 1951.
- [4] B. Sridhar Babu, A. Kumaraswamy and B. A. Prasad, "Investigation of elasto-plastic deformation behavior of Haynes 242 alloy subjected to nanoscale loads through indentation experiments." *Trans. Indian Inst. Met.*, vol. 69, no. 3, pp. 759-766, 2016, doi: 10.1007/s12666-015-0550-8.
- [5] K. Eswar Prasad, N. Chollacoop and U. Ramamurty "Role of indenter angle on the plastic deformation underneath a sharp indenter and on representative strains: An experimental and numerical study," *Acta Mater.*, vol. 59, pp. 4343–4355, 2010, doi: 10.1016/j.actamat.2011.03.058.
- [6] B. Sridhar Babu, and Kaushik Kumar, "Temperature dependence of indentation behavior of ti-6al-4v alloy for bio medical applications," *Biointerface Res. Appl. Chem.*, vol. 9, no. 6, pp. 4629–4634, 2019, doi: 10.33263/BRIAC96.629634.
- [7] E.D. Hintsala, U. Hagen, D.D. Stauffer, "High-throughput nanoindentation for statistical and spatial property determination," *J. Mater.*, vol. 70, pp. 494–503, 2018, doi: 10.1007/s11837-018-2752-0.
- [8] Eswar Prasad K Raghavan K and Ramamurty U, "Temperature dependence of pressure sensitivity in a metallic glass," *Scr. Mater.*, 57, pp.121-125, 2007, doi: 10.1016/j.scriptamat.2007.03.033.
- [9] C. Moussa *et al.*, "Characterization of homogenous and plastically graded materials with spherical indentation and inverse analysis," *J. Mater. Res.*, vol. 27, pp. 20-27, 2012, doi: 10.1557/jmr.2011.303.
- [10] P. Sudharshan Phani, and W.C. Oliver, "A critical assessment of the effect of indentation spacing on the measurement of hardness and modulus using instrumented indentation testing," *Mater. Des.*, vol. 164, p. 107563, 2019, doi: 10.1016/j.matdes.2018.107563.
- [11] P. Brammer *et al.*, "A method to take account of the geometrical imperfections of quasi-spherical indenters," *Mater. Des.*, vol. 49, pp. 406–413, 2013, doi: 10.1016/j.matdes.2013.01.028

- [12] S. Khammassi *et al.*, “Poly (lactic acid)(pla)-based nanocomposites: impact of vermiculite, silver, and graphene oxide on thermal stability, isothermal crystallization, and local mechanical behavior,” *J. Compos. Sci.*, vol. 6, no. 4, pp. 112, 2022, doi: 10.3390/jcs6040112.
- [13] S. Khammassi, M. Tarfaoui and K. Lafdi, “Study of mechanical performance of polymer nanocomposites reinforced with exfoliated graphite of different mesh sizes using micro-indentation,” *J. Compos. Sci.*, vol. 55, no. 19, pp. 2617-2629, 2021, doi: 10.1177/0021998321993211.
- A. Bolshakov, and G. M. Pharr, “Influences of pile-up on the measurement of mechanical properties by load and depth-sensing indentation techniques,” *J. Mater. Res.*, vol. 13, no. 4, pp. 1049 – 1058, 1998, doi: 10.1557/JMR.1998.0146.
- [14] P. Sudharshan Phani, and W.C. Oliver, “Ultra high strain rate nanoindentation testing,” *Materials (Basel)*, vol. 10, pp. 663–674, 2017, doi: 10.3390/ma10060663.
- [15] B. R. Donohue, A. Ambrus and S. R. Kalidindi, “Critical evaluation of the indentation data analyses methods for the extraction of isotropic uniaxial mechanical properties using finite element models,” *Acta Materialia*, vol. 60, pp. 3943–3952, 2012, doi: 10.1016/j.actamat.2012.03.034.
- [16] M. Beghini, L. Bertini and V. Fontanari, “Evaluation of the stress-strain curve of metallic materials by spherical indentation,” *Int. J. Solids Struct.*, vol. 43, pp. 2441-2459, 2006, doi: 10.1016/j.ijsolstr.2005.06.068.
- [17] E.P. Koumoulos *et al.*, “Metrology and nanomechanical tests for nano-manufacturing and nano-bio interface: challenges & future perspectives,” *Mater. Des.*, vol. 137, pp.446–462, 2018, doi: 10.1016/j.matdes.2017.10.035S.
- [18] Syngellakis, *et al.*, “Finite element simulation of spherical indentation experiments,” *Int. J. Comp. Meth. and Exp. Meas.*, vol. 6, pp. 749-763, 2018, doi: 10.2495/CMEM-V6-N4-749-763.
- [19] G. Cao, and T. Niu, “Finite element modeling of the indentation behavior of two-dimensional materials,” *Acta Mech.*, vol. 230, pp. 1367–1376, 2019, doi: 10.1007/s00707-017-2020-3.
- [20] G. Cao, and T. Niu, “Finite element modeling of the indentation behavior of two-dimensional materials,” *Acta Mech.*, vol. 230, pp. 1367–1376, 2019, doi: 10.1007/s00707-017-2020-3.